Solar Energy Materials & Solar Cells 149 (2016) 75–80

Contents lists available at ScienceDirect

Solar Energy Materials & Solar Cells

journal homepage: www.elsevier.com/locate/solmat

Cerium oxide and hydrogen co-doped indium oxide films for high-efficiency silicon heterojunction solar cells

Eiji Kobayashi [a,b,*], Yoshimi Watabe [a], Tetsuya Yamamoto [c], Yoichi Yamada [b]

[a] Choshu Industry Co., Ltd., 3740, Shin-yamanoi, Sanyo Onoda, Yamaguchi 757-8511, Japan
[b] Department of Materials Science and Engineering, Yamaguchi University, 2-16-1 Tokiwadai, Ube, Yamaguchi 755-8611, Japan
[c] Research Institute, Kochi University of Technology, 185 Miyanokuchi, Tosayamada-cho, Kami-shi, Kochi 782-8502, Japan

ARTICLE INFO

Article history:
Received 1 October 2015
Received in revised form
22 December 2015
Accepted 4 January 2016
Available online 22 January 2016

Keywords:
Silicon heterojunction
Solar cell
Transparent conductive oxide
Indium oxide
Cerium oxide
Mobility

ABSTRACT

CeO_2 and hydrogen co-doped In_2O_3 (ICO:H) films deposited by ion plating with dc arc-discharge were used as a transparent conducting oxide (TCO) electrode in hydrogenated amorphous silicon (a-Si:H)/crystalline silicon (c-Si) heterojunction (SHJ) solar cells. Incorporating ICO:H instead of conventional Sn-doped In_2O_3 (ITO) films and hydrogenated In_2O_3 (IO:H) films, improved the fill factor (*FF*) and short-circuit current density (J_{sc}) simultaneously. The best SHJ cell (243.4 cm^2) containing ICO:H films had a conversion efficiency of 24.1%, open-circuit voltage of 745 mV, J_{sc} of 38.8 mA/cm^2, and *FF* of 83.2% because of their high Hall mobility of 140 cm^2/V s. We have clarified the following design principles for ICO:H films: (i) the Ce species substituted for In atoms acts as a donor and (ii) CeO_2 and H decrease the residual strain and the contribution of the grain boundary scattering to carrier transport. This co-doping method can produce high conversion efficiencies in all solar cells containing TCO with resistive emitters.

1. Introduction

Hydrogenated amorphous silicon (a-Si:H)/crystalline silicon (c-Si) heterojunction (SHJ) solar cells are currently the focus of much research because they can achieve very high conversion efficiencies with simple processes [1–15]. The highest reported short-circuit current density (J_{sc}), open-circuit voltage (V_{oc}), and fill factor (*FF*) for this type of cell are 40.1 mA/cm^2, 750 mV, and 0.832, respectively [1]. As for all solar cells with resistive emitters, the conversion efficiency of SHJ solar cells is increased by low electrical resistivity and low optical absorption loss at wavelengths from the visible to the near-infrared (NIR) spectral regions of the transparent conducting oxide (TCO) layers. Although Sn-doped In_2O_3 (ITO) films have been widely used in solar cells [16,17], the light absorption loss in the TCO layers in the NIR region arising from free carrier absorption (FCA), which results from the high carrier density (*N*) causing plasma oscillations, must be addressed for light management [18]. In addition, the thermal stability of SHJ cells is usually limited to 200 or 250 °C [19,20]. Therefore, high-mobility TCO films deposited at temperatures below 200 °C must be compatible with high current properties and low ohmic losses without degrading the passivation properties.

Various metals have been used to dope polycrystalline In_2O_3 films to decrease the intragrain defects. W [21–23], Zr [24,25], Mo [26,27], Ti [28]-doped In_2O_3 films show high Hall mobility (μ_H) exceeding 80 cm^2/V s. In addition, Koida et al. showed that highly H-doped In_2O_3 (IO:H) films obtained by using H_2O vapor exhibited μ_H exceeding 100 cm^2/V s and good transparency in the NIR region [29–32]. Libera et al. reported the performance of IO:H films deposited by atomic layer deposition at 100–250 °C with O and H_2O vapor [33], similar to IO:H films produced by Koida. Although the electrical resistivity (ρ) in highly H-doped ITO films is decreased [34], doping pure In_2O_3 with H is more effective for decreasing the intragrain defects compared with conventional ITO. *N* of IO:H films [29–32] containing more than 2 atom % H exceeds 1.0×10^2 cm^{-3} because the H atoms act as shallow donors [35,36].

We have reported 100-nm-thick CeO_2-doped hydrogenated In_2O_3 (ICO:H) films with superior μ_H values of 130–145 cm^2/V s and low *N* values of less than 3×10^{20} cm^{-3} [37]. Our strategy of co-doping with CeO_2 and H is based on two factors [37]. (i) The effective ionic radius of tetravalent Ce donors with a coordination number of 6 (0.101 nm) is close to that of trivalent In with a coordination number of 6 (0.094 nm) [38], producing little change in microstrain around the dopant sites. (ii) The density of O vacancies (V_O) can be decreased by doped CeO_2 with a large standard enthalpy of formation compared with In_2O_3, improving the crystallinity. Analyzing the relationship between μ_H and *N* of ICO:H films showed that the main factor limiting the carrier

* Corresponding author. Tel.: +81 836 711055; fax: +81 836 711056.
E-mail address: kobayashi.eiji@choshu.co.jp (E. Kobayashi).

http://dx.doi.org/10.1016/j.solmat.2016.01.005
0927-0248/

transport of the films is the intragrain ionized impurity scattering mechanism [37].

Here, we report the advantages of SHJ solar cells containing ICO:H films over the solar cells with conventional TCO films. We show that ICO:H films improve *FF* and J_{sc} simultaneously compared with conventional ITO films and IO:H films. We fabricated SHJ solar cells with an efficiency of 24.1% after fully optimizing all process steps. In addition, we propose the design principles for ICO:H films with superior μ_H based on Ce L_3 X-ray absorption near edge structure (XANES) spectra measurements and analysis of those films.

2. Materials and methods

ICO:H films were deposited by ion plating with dc arc-discharge, also called high-density plasma-enhanced evaporation (HPE) [39,40], at a low growth temperature of 150 °C. Commercially, HPE is suitable for depositing TCO layers in high-efficiency SHJ solar cells because its ion bombardment is lower than conventional sputtering, and its growth rate of typically 5.5 nm/s in our experimental setup is high. The ultimate vacuum pressure of the process chamber before the deposition was 6.0×10^{-5} Pa. The deposition gases were Ar, O_2, and H_2. The total gas pressure during film deposition was 0.45 Pa.

Intentionally introduced H_2O vapor during TCO-film growth is generally used to incorporate H atoms into the TCO films deposited by sputtering. Residual H_2O vapor in the deposition chamber with HPE and conventional sputtering can affect the film properties. We monitored the gas during deposition using a quadrupole mass spectrometer (Prisma Plus QMG220, Pfeiffer Vacuum) with an ultra-high-vacuum differential pumping system at an ultimate partial pressure of H_2O of 10^{-7} Pa to investigate the effect of residual gas in a chamber. Fig. 1 shows the partial pressure of H_2O vapor (P_{H_2O}) and H_2 (P_{H_2}) during discharge as a function of H_2 gas flow ratio (Q_H). The O_2 gas flow ratio was fixed at 11%. The P_{H_2O} values were calculated from the spectrum peak of the mass-to-charge ratio (m/z) of 18, which eliminated the effect of the doublet ion of the argon isotope $^{36}Ar^{2+}$. H_2O vapor in the residual gas, with a P_{H_2O} of 1.6×10^{-4} Pa, acted as a H source during deposition. P_{H_2} increased slightly with increasing Q_H, in contrast to P_{H_2O}. Although H_2O vapor was used as a H source during sputtering deposition, this result suggests that H_2 gas can be used for H doping the TCO films by HPE. Using H_2 gas instead of H_2O vapor has the advantage that a complex system for deaerating H_2O vapor to exclude carbon dioxide and avoid contamination is unnecessary. HPE uses arc discharge at a high pressure of around 100 Pa, whereas sputtering uses glow discharge at a low pressure of around 1 Pa. Arc discharge at a high pressure can produce a dc arc plasma with a low electron temperature (T_e) compared with glow plasma [41]. As T_e increases, the ion bombardment of the substrate increases with the difference in the potential between plasma and substrate. We speculate that high-energy hydrogen ions generated by glow discharge with high T_e increase the number of dangling bonds in TCO films, increasing the strain in the films. Consequently, using H_2 gas in HPE at low T_e produces high-quality TCO films, in contrast to conventional sputtering.

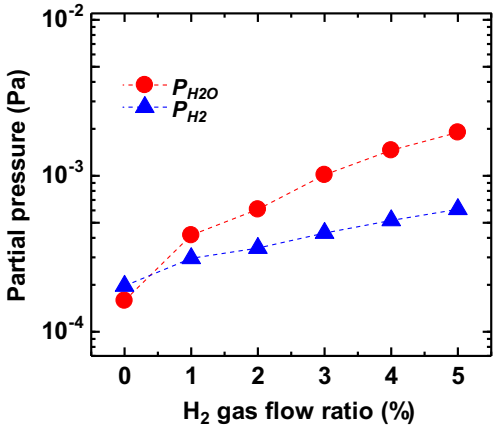

Fig. 1. Partial pressure of water vapor (P_{H_2O}) and H_2 (P_{H_2O}) as a function of Q_H during discharge.

The source materials for TCO deposition in this study were pure In_2O_3, and In_2O_3 pellets containing 3% CeO_2 (ICO), 10% SnO_2, or 1% WO_3 (IWO). All pellets were produced by Sumitomo Metal Mining Co., Ltd. The ICO:H, ITO and IO:H films were deposited on glass substrates (EAGLE XG, Corning) for electrical and optical characterization and structural analysis. The film compositions were analyzed by Rutherford backscattering spectrometry (RBS) and hydrogen forward scattering (HFS) with a custom-built RBS system from CEA. Electric conductivity and Hall voltage were measured with a Hall effect measurement system (ResiTest 8300, Toyo Technica). To analyze the optical band gap and assess the absorbance in the NIR region of TCO films, optical spectra were measured at wavelengths from 250 to 2500 nm with a grating spectrometer (V-770, JASCO). The chemical states of Ce dopants in ICO:H and non-H doped ICO films were evaluated from L_3-XANES spectra. Ce L_3-XANES spectra were obtained by the conversion He^+ yield method at BL11 of Kyushu Synchrotron Light Research Center [42]. The measurements were carried out at energy intervals of about 0.19 eV.

The cell structure was metal grid/TCO/a-Si:H *p*/a-Si:H *i*/c-Si *n*/a-Si:H *i*/a-Si:H *n*/TCO/blanket metal. The cell size was 243.4 cm^2. Both sides of the TCO layer were deposited with the same materials and process conditions. The thicknesses of the a-Si:H layers and TCO layer on each side of the wafers were approximately 10 and 70 nm, respectively. The total thickness of the a-Si:H layers was determined by transmission electron microscope measurements.

We used Czochralski (CZ) wafers as absorbers for the SHJ solar cells. The Si(100) wafers had a ρ of 2.0 Ω cm. The as-grown wafers were textured in alkaline solution and wet-chemically cleaned before they underwent thermal donor killer annealing. The textured wafers were dipped in 5% HF solution just before plasma-enhanced chemical vapor deposition (PECVD). The final wafer thickness of the CZ Si was approximately 130 μm. The SHJ solar cells contained thin a-Si:H films as a wide gap layer on both sides of the c-Si wafers that passivated the front heterojunction emitter, which collects minority-carriers, and the back contact, which collects majority-carriers. Intrinsic and doped a-Si:H layers were deposited on the whole wafer surfaces at 150–200 °C using mixtures of SiH_4, PH_3, B_2H_6, and H_2 in an automated parallel-plate industrial PECVD reactor at 40.68 MHz. TCO films were deposited by HPE on the front and back of the solar cells. Silver reflectors were deposited on the back of the cells by sputtering. Front fingers with no busbars were screen-printed with low-temperature silver paste. Finally, the cells were cured at 200 °C for 30 min.

The *J–V* characteristics of SHJ cells were measured with a Spot^{LIGHT} cell tester with a Grid^{TOUCH} contacting system (Pasan, Meyer Burger Technology Ltd.). The Grid^{TOUCH} system ensured a homogeneous pressure distribution across all fingers for *FF* measurement via its slightly bent bottom plate and an adapted load on the 35 wires perpendicular to the cell fingers. The voltage measurement was carried out using 5 of the 35 wires, distributed over the entire cell, while the other 30 were used to extract the current. J_{sc} was inversely proportional to the number of wires because of the shadowing effect of the wires on the cell. J_{sc} with no

shadowing effect from the contacting system was extrapolated by compensating for the wire shadows [43]. The spectral response and internal quantum efficiency (IQE) were determined from the external quantum efficiency and reflectance measurements (CEP-25RR, Bunkokeiki).

3. Results and discussions

Fig. 2 shows the maximum output power (P_{max}), J_{sc}, V_{oc}, and *FF* of SHJ cells containing different TCO films. Each characteristic value is normalized at the characteristic value of the ICO:H cell. The characteristics of the TCO films in Fig. 2 and the ICO film are summarized in Table 1. The plasma wavelength (λ_{pe}) of the TCO films is given by

$$\lambda_{pe} = \frac{1}{\omega_{pe}} = \sqrt{\frac{\varepsilon m^*}{nq^2}} \quad (1)$$

where ω_{pe} is the plasma frequency, ε is the permittivity, m^* is the electron effective mass, and q is the carrier charge. By using Eq. (1), the λ_{pe} values in Table 1 for TCO films were calculated assuming that $\varepsilon = 4.0\varepsilon_0$ [44], where ε_0 is the vacuum permittivity, and $m^* = 0.3m_0$, where m_0 is the free electron rest mass [18]. The attenuation constant of TCO films as a function of wavelength (λ) increased at around λ_{pe} because of plasma oscillation, a phenomenon known as "cut-off" [44].

Fig. 3 shows the normalized J_{sc} of SHJ cells as a function as λ_{pe}. The SHJ cells in Fig. 3 show a strong correlation between J_{sc} and λ_{pe}. Although the ITO films had a wide optical band gap caused by the Burstein–Moss shift arising from high N, J_{sc} of the ITO cells was decreased by FCA of ITO films at around λ_{pe}. This observation was consistent with the IQE spectra and reflectance spectra of the SHJ solar cells containing ICO:H and ITO films (Fig. 4). The ICO:H cells had high IQE in the NIR region, whereas they also had high reflectance in the same spectral region owing to the lower FCA of ICO:H films with lower N. The low IQE of the ITO cells compared with the ICO:H cells at a given λ (Fig. 4) was caused by the FCA arising from high N.

The *FF* of ICO:H cells with Q_H of 1.0%, and ITO cells and IO:H cells with Q_H of 1.0% decreased as ρ of the TCO films improved. Consequently, the highest *FF* was obtained in ICO:H cells. However, the *FF* of IO:H cells with Q_H of 2.0% was substantially lower, despite the increase in ρ of those films. To verify the effect of Q_H during deposition on *FF*, we fabricated SHJ cells with TCO films with similar ρ values. We used IWO films to obtain similar ρ values of 0.26–0.29 mΩ cm with different Q_H. Fig. 5 shows the normalized

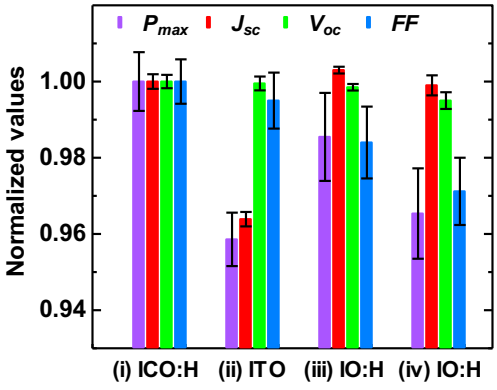

Fig. 2. Normalized P_{max}, J_{sc}, V_{oc}, and *FF* of SHJ cells containing (i) ICO:H films with Q_H of 1.0%, (ii) ITO films with Q_H of 0%, (iii) IO:H with Q_H of 1.0%, and (iv) IO:H with Q_H of 2.0%. Each value is normalized to the corresponding value of the ICO:H cell. Error bars represent the standard deviation.

FF of SHJ cells as a function of Q_H. The *FF* values decreased as Q_H increased above 1%. All SHJ cells in Fig. 5 had a shunt resistance of > 10 kΩ, which indicates little effect on the *FF*; therefore, the reduction of *FF* with increasing Q_H was caused by an increase in series resistance in the SHJ cells.

Barraud et al. reported that SHJ cells containing IO:H films have a lower *FF* owing to poor contact between the silver fingers and the IO:H layer for $P_{H_2O} > 0.8$ mPa [7]. However, no difference in contact resistance (< 1 mΩ cm^2) between the IO:H film and silver fingers was observed for our cells containing IO:H with Q_H of 1.0% ($P_{H_2O} = 0.42$ mPa) and IO:H with Q_H of 2.0% ($P_{H_2O} = 0.61$ mPa) on a textured Si wafer measured by the transmission line method. This may be because H radicals degrade the surfaces of *n*- and *p*-doped a-Si:H layers during TCO deposition, increasing the contact resistance between doped a-Si:H/TCO by plasma damage. In addition, the plasma density could change with Q_H; IO:H with Q_H of 1.0% underwent an increase in the deposition rate of approximately 10% compared with pure In_2O_3 with Q_H of 0%. The discharge voltage of the arc-plasma did not change with Q_H. Therefore, TCO films with Q_H of ≤ 1.0% deposited by HPE increased the conversion efficiency of the SHJ structure. The ICO:H films with Q_H of 1.0% satisfied this requirement. The design principles of CeO_2 and H co-doping are discussed below.

As shown in Fig. 6, we fabricated a 243.4 cm^2 SHJ solar cell with a conversion efficiency of 24.1% using ICO:H films after optimizing the texture, a-Si:H layers, metal contact, and grid design [15]. The V_{oc} of 745 mV and *FF* of 0.832 in the ICO:H cell and efficiency of 24.1% are comparable to those for the best SHJ solar cells fabricated by Panasonic Corporation [1]. However, J_{sc} of 38.8 mA/cm^2 in the ICO:H cell is lower than that of 40.1 mA/cm^2 in the Panasonic cell with busbars, even though the ICO:H cell has no busbars. This result suggests that the narrow grid design must be improved to create an SHJ solar cell with a higher cell efficiency of 25%. One promising approach to reach this goal is Cu electroplating instead of screen printing.

Next, we discuss the characteristics of the TCO films developed in this study to demonstrate our design strategy for TCO films that can produce high-performance SHJ solar cells. We measured the Ce L_3-XANES spectra of ICO:H films with Q_H of 1.0%, ICO films with Q_H of 0%, and a reference sample of pressed CeO_2 (Sumitomo Metal Mining Co., Ltd.) with boron nitride to determine the valence states of Ce dopants (Fig. 7). The spectra of the ICO:H and ICO film show three major peaks and possess similar shapes [45–48], which can be fitted by a combination of an arctangent and several Lorentzian functions (Fig. 8). Peak A is ascribed to trivalent Ce atoms with a final state of $2p4f^{1}5d^*$, where $2p$ and $5d^*$ denote a $2p$ core hole and the excited electron in the previously unoccupied $5d$ state, respectively. Peaks B and C are ascribed to tetravalent Ce species with final states of L4 $f^{1}5d^*$ and L4 $f^{0}5d^*$, respectively, where L refers to the hole in $2p$ shell. The low-energy shoulder D arises because of the crystal-field splitting of the Ce $5d$ states. The peak energy positions of peaks B and C were consistent with the reference CeO_2 sample. We calculated the charge states of Ce dopants in the ICO:H film and the ICO film from the area ratio of each spectrum component of trivalent Ce and tetravalent Ce. The calculated Ce charge states in the ICO:H and ICO film were 3.12 and 3.32, respectively. From our findings, we concluded that Ce atoms used as dopants replace In atoms in the ICO:H and ICO films. The dominant valence states of Ce species were 3+ and 4+ in those films.

RBS and HFS measurements showed that the ICO:H film with Q_H of 1.0% had a composition of 35.7% In, 0.6% Ce, 62.4% O, and 1.3% H, and that the ICO film deposited with Q_H of 0% had a composition of 34.0% In, 0.7% Ce, 64.6% O, and 0.7% H [37]. Both ICO and ICO:H films were O-rich, in contrast to the stoichiometric composition of In_2O_3. This confirmed that the effect of Ce doping on

Table 1
Electrical and optical properties of ICO:H film with Q_H of 1.0%, ICO film with Q_H of 0%, ITO film with Q_H of 0%, IO:H film with Q_H of 1.0%, and IO:H film with Q_H of 2.0%.

TCO Material	H_2 gas flow ratio Q_H	Resistivity ρ ($\times 10^{-4}$ Ω cm)	Carrier density N ($\times 10^{20}$ cm^{-3})	Hall mobility μ_H (cm^2/V s)	Plasma wavelength λ_{pe} (μm)	Optical band gap E_{opt} (eV)
ICO:H	1.0%	2.21	2.01	141	2.58	3.84
ICO	0%	4.07	1.93	79.3	2.63	3.82
ITO	0%	2.48	9.72	25.9	1.17	4.24
IO:H	1.0%	5.60	1.20	92.8	3.34	3.77
IO:H	2.0%	3.19	1.87	105	2.67	3.81

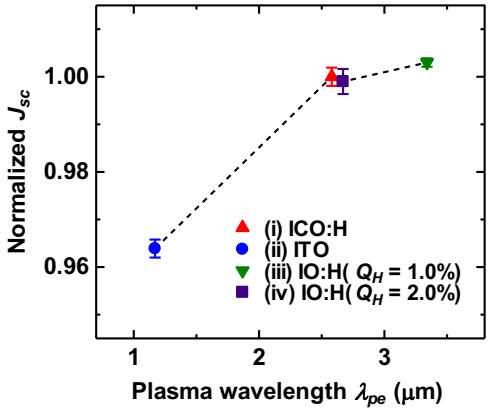

Fig. 3. Normalized J_{sc} of SHJ cells containing (i) ICO:H films with Q_H of 1.0%, (ii) ITO films with Q_H of 0%, (iii) IO:H with Q_H of 1.0%, and (iv) IO:H with Q_H of 2.0% as a function of λ_{pe}.

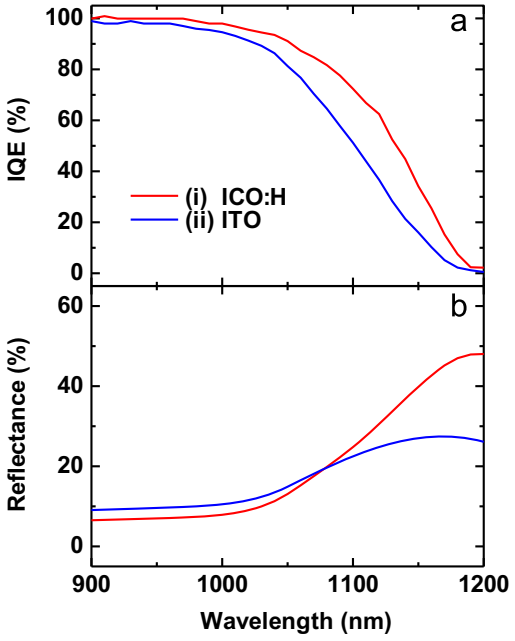

Fig. 4. (a) IQE and (b) reflectance spectra as a function of wavelength of SHJ cells containing (i) ICO:H films with Q_H of 1.0% and (ii) ITO films with Q_H of 0%.

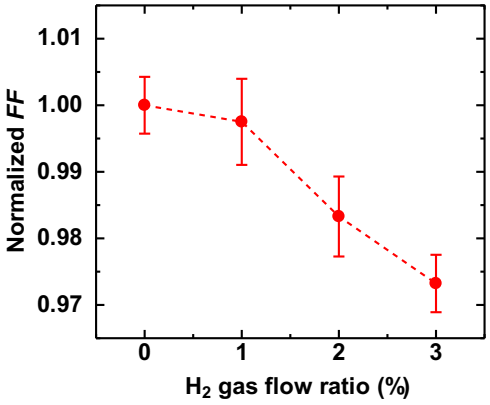

Fig. 5. Normalized FF of SHJ cells with TCO films with ρ values from 0.26 to 0.29 mΩ cm as a function of Q_H. Each value is normalized to the corresponding value of the cell containing films with Q_H of 0%. Error bars represent the standard deviation.

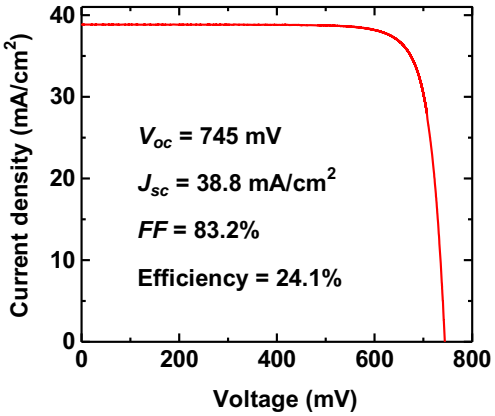

Fig. 6. Current density–voltage characteristics of our best SHJ cell comprising ICO:H films.

the O composition of the films was to decrease the density of the intra-granular V_O. It is necessary to control the O composition, because O interstitials (O_i) with electron affinity would act as *n*-type killer defects. Furthermore, In vacancy (V_{In}) and O-related defects, such as O_i, within the grains, and chemisorbed O species at the grain boundaries with a negative charge (O^-), would form a barrier, causing free-carrier scattering that would decrease the carrier mobility. Based on the Ce L_3-XANES results, we concluded that co-doping with CeO_2 and H decreases the number of tetravalent Ce at In sites and suppresses the generation of the *n*-type killer defects. The co-doping plays an important role in decreasing the microstrain in the films that originates in the various point defects and the passivation of grain boundaries.

Fig. 9 shows ρ, *N*, and μ_H of the ICO:H and ICO films as functions of the O_2/Ar ratio. ICO:H films showed high μ_H values ranging from 130 to 145 cm^2/V s and a relatively low *N* of 2.0×10^{20} cm^{-3}. The density of tetravalent Ce in ICO:H films was lower than that of ICO films. This could cause the low *N* of ICO:H films compared with that of ICO films. However, we found a small difference in *N* between the two films (Fig. 9). We considered the following two explanations for this observation: (i) the reduction in the carrier-trap sites at the grain boundaries and the decrease in the intra-grain compensation ratio; and (ii) intragrain H species in ICO:H films, which act as shallow donors [35,36]. Explanation (i) explains

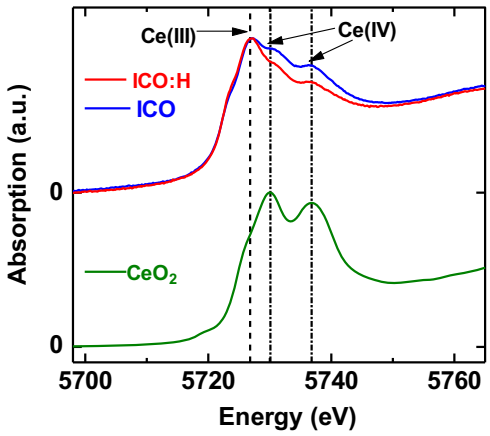

Fig. 7. Ce L_3-XANES spectra of the ICO:H film with Q_H of 1%, the ICO film with Q_H of 0%, and the pressed CeO_2 pellet with boron nitride. The background has been removed. The zero of the energy scale is fixed at the first main absorption feature.

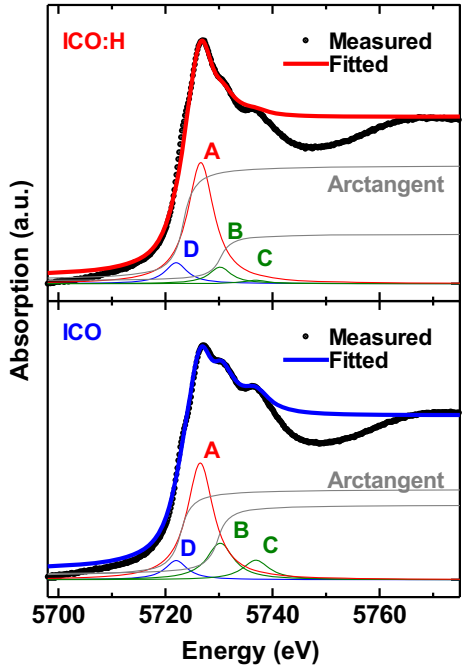

Fig. 8. Ce L_3-XANES spectra and fittings (thick lines) with an arctangent curve and a Lorentzian function (thin lines) of the ICO:H films with Q_H of 1% (red) and of ICO films with Q_H of 0% (blue). (For interpretation of the references to color in this figure legend, the reader is referred to the web version of this article.)

the remarkable increase in μ_H shown in Fig. 9. We have no data that confirm the presence of the H donors, and further study is needed.

4. Conclusions

We have demonstrated that a commercial-sized SHJ cell (243.4 cm^2) containing ICO:H films has a high conversion efficiency of 24.1%. The ICO:H cells have several advantages over IO:H or conventional ITO cells: (i) the ICO:H cells have high *FF* of more than 83% and a high J_{sc} of 38.8 mA/cm^2 because of the high μ_H of 140 cm^2/V s and low N of 2.0×10^{20} cm^{-3}; and (ii) ICO:H films with low Q_H exhibit high μ_H compared with IO:H films, decreasing the *FF* of SHJ cells. Based on the Ce valence states and compositions of ICO:H films, we have elucidated the design principles of ICO:H films: (i) Ce and In-substituting species, acts as donors; and

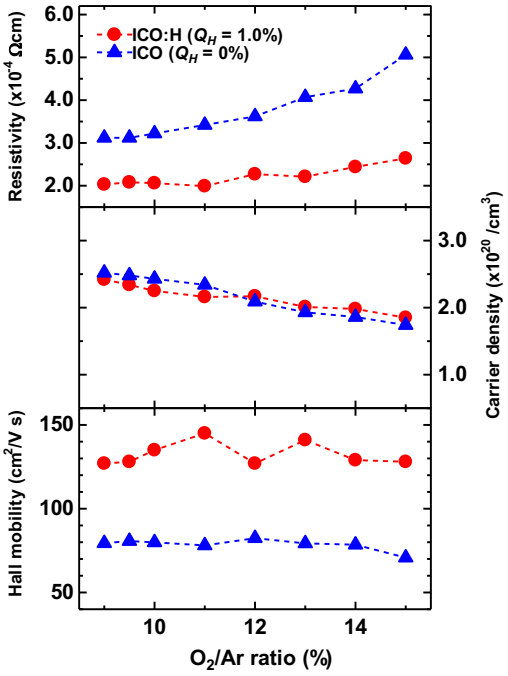

Fig. 9. Electrical resistivity, carrier density, and Hall mobility of ICO:H films with Q_H of 1% and ICO films as a function of O_2/Ar ratio.

(ii) CeO_2 and H decrease the residual strain and the contribution of the grain boundary scattering to the carrier transport. The findings prove that ICO:H films and their design have great potential for applications in all solar cells with resistive emitters.

Acknowledgment

The authors would like to thank the following people for their excellent work in cell preparation: Mr. Kimikazu Hashimoto, Mr. Seiji Sato, Mr. Fumiharu Ishimura, Mr. Yasunori Hase, Ms. Yuka Kuroiwa, and Ms. Mai Hayashi. The experiments using synchrotron radiation were performed at the beamlines BL11 of the SAGA Light Source with the approval of the Kyushu Synchrotron Light Research Center (Proposal No. 1404020ST and 1503019S).

References

[1] M. Taguchi, A. Yano, S. Tohoda, K. Matsuyama, Y. Nakamura, T. Nishiwaki, K. Fujita, E. Maruyama, 24.7% record efficiency HIT solar cell on thin silicon wafer, IEEE J. Photovolt. 4 (1) (2013) 96–99.
[2] K. Masuko, M. Shigematsu, T. Hashiguchi, D. Fujishima, M. Kai, N. Yoshimura, T. Yamaguchi, Y. Ichihashi, T. Mishima, N. Matsubara, T. Yamanishi, T. Takahama, M. Taguchi, E. Maruyama, S. Okamoto, Achievement of more than 25% conversion efficiency with crystalline silicon heterojunction solar cell, IEEE J. Photovolt. 4 (6) (2014) 1433–1435.
[3] T. Mishima, M. Taguchi, H. Sakata, E. Maruyama, Development status of high-efficiency HIT solar cells, Sol. Energy Mater. Sol. Cells 95 (2011) 18–21.
[4] Qi Wang, M.R. Page, E. Iwaniczko, Y. Xu, L. Roybal, R. Bauer, B. To, H.-C. Yuan, A. Duda, F. Hasoon, Y.F. Yan, D. Levi, D. Meier, H.M. Branz, T.H. Wang, Efficient heterojunction solar cells on p -type crystal silicon wafers, Appl. Phys. Lett. 96 (2010) 013507.
[5] J.P. Seif, A. Descoeudres, M. Filipič, F. Smole, M. Topič, Z.C. Holman, S. De Wolf, C. Ballif, Amorphous silicon oxide window layers for high-efficiency silicon heterojunction solar cells, J. Appl. Phys. 115 (2014) 024502.
[6] C. Battaglia, S.M. de Nicolás, S. De Wolf, X. Yin, M. Zheng, C. Ballif, A. Javey, Silicon heterojunction solar cell with passivated hole selective MoOx contact, Appl. Phys. Lett. 104 (2014) 113902.
[7] L. Barraud, Z.C. Holman, N. Badel, P. Reiss, A. Descoeudres, C. Battaglia, S. De Wolf, C. Ballif, Hydrogen-doped indium oxide/indium tin oxide bilayers for high-efficiency silicon heterojunction solar cells, Sol. Energy Mater. Sol. Cells 115 (2013) 151–156.

[8] Z.C. Holman, A. Descoeudres, L. Barraud, F.Z. Fernandez, J.P. Seif, S. De Wolf, C. Ballif, Current losses at the front of silicon heterojunction solar cells, IEEE J. Photovolt. 2 (1) (2012) 7–15.

[9] M. Bivour, S. Schröer, M. Hermle, S.W. Glunz, Silicon heterojunction rear emitter solar cells: less restrictions on the optoelectrical properties of front side TCOs, Sol. Energy Mater. Sol. Cells 122 (2014) 120–129.

[10] R. Varache, O.N. Aguila, A. Valla, N. Nguyen, D. Munoz, Role of the front electron collector in rear emitter silicon heterojunction solar cells, IEEE J. Photovolt. 5 (3) (2015) 711–717.

[11] T.F. Schulze, L. Korte, F. Ruske, B. Rech, Band lineup in amorphous/crystalline silicon heterojunctions and the impact of hydrogen microstructure and topological disorder, Phys. Rev. B 83 (2011) 165314.

[12] M. Mews, M. Liebhaber, B. Rech, L. Korte, Valence band alignment and hole transport in amorphous/crystalline silicon heterojunction solar cells, Appl. Phys. Lett. 107 (2015) 013902.

[13] T. Watahiki, T. Furuhata, T. Matsuura, T. Shinagawa, Y. Shirayanagi, T. Morioka, T. Hayashida, Y. Yuda, S. Kano, Y. Sakai, H. Tokioka, Y. Kusakabe, H. Fuchigami, Rear-emitter Si heterojunction solar cells with over 23% efficiency, Appl. Phys. Express 8 (2015) 021402.

[14] G. Coletti, Y. Wu, G. Janssen, J. Loffler, B.B. van Aken, F. Li, Y. Shen, W. Yang, J. Shi, G. Li, Z. Hu, J. Xiong, 20.3% MWT Silicon heterojunction solar cell-a novel heterojunction integrated concept embedding low Ag consumption and high module efficiency, IEEE J. Photovolt 5 (1) (2015) 55–60.

[15] E. Kobayashi, Y. Watabe, R. Hao, T.S. Ravi, High efficiency heterojunction solar cells on n-type kerfless mono crystalline silicon wafers by epitaxial growth, Appl. Phys. Lett. 106 (2015) 223504.

[16] H. Kobayashi, T. Ishida, Y. Nakato, H. Tsubomura, Mechanism of carrier transport in highly efficient solar cells having indium tinoxide/Si junctions, J. Appl. Phys. 69 (1991) 1736.

[17] T. Kamimori, J. Nagai, M. Mizuhashi, Electrochromic devices for transmissive and reflective light control, Sol. Energy Mater. 16 (1987) 27–38.

[18] I. Hamberg, C.G. Granqvist, Evaporated Sn-doped In_2O_3 films: Basic optical properties and applications to energy-efficient windows, J. Appl. Phys. 60 (1986) R123.

[19] L. Zhao, Z. Zhou, H. Peng, R. Cui, Indium tin oxide thin films by bias magnetron rf sputtering for heterojunction solar cells application, Appl. Surf. Sci. 252 (2005) 385–392.

[20] V.A. Dao, H. Choi, J. Heo, H. Park, K. Yoon, Y. Lee, Y. Kim, N. Lakshminarayan, J. Yi, rf-Magnetron sputtered ITO thin films for improved heterojunction solar cell applications, Curr. Appl. Phys. 10 (2010) S506–S509.

[21] M. Yang, J. Feng, G. Li, Q. Zhang, Tungsten-doped In_2O_3 transparent conductive films with high transmittance in near-infrared region, J. Cryst. Growth 310 (2008) 3474–3477.

[22] Y. Abe, N. Ishiyama, Polycrystalline films of tungsten-doped indium oxide prepared by d.c. magnetron sputtering, Mater. Lett. 61 (2007) 566–569.

[23] P.F. Newhouse, C.-H. Park, D.A. Keszler, J. Tatea, P.S. Nyholm, High electron mobility W-doped In_2O_3 thin films by pulsed laser deposition, Appl. Phys. Lett. 87 (2005) 112108.

[24] T. Koida, M. Kondo, High-mobility transparent conductive Zr-doped In_2O_3, Appl. Phys. Lett. 89 (2006) 082104.

[25] T. Koida, M. Kondo, Improved near-infrared transparency in sputtered In2O3 -based transparent conductive oxide thin films by Zr-doping, J. Appl. Phys. 101 (2007) 063705.

[26] Y. Meng, X. Yang, H. Chen, J. Shen, Y. Jiang, Z. Zhang, Z. Hua, A new transparent conductive thin film In O:Mo, Thin Solid Films 394 (2001) 219–223.

[27] W. Miao, X. Li, Q. Zhang, L. Huang, Z. Zhang, L. Zhang, X. Yan, Transparent conductive In_2O_3:Mo thin films prepared by reactive direct current magnetron sputtering at room temperature, Thin Solid Films 500 (2006) 70–73.

[28] M.F.A.M. van Hest, M.S. Dabney, J.D. Perkins, D.S. Ginley, M.P. Taylor, Titanium-doped indium oxide: a high-mobility transparent conductor, Appl. Phys. Lett. 87 (2005) 032111.

[29] T. Koida, H. Fujiwara, M. Kondo, Hydrogen-doped In_2O_3 as high-mobility transparent conductive oxide, Jpn. J. Appl. Phys. 46 (2007) L685–L687.

[30] T. Koida, H. Fujiwara, M. Kondo, Reduction of optical loss in hydrogenated amorphous silicon/crystalline silicon heterojunction solar cells by high-mobility hydrogen-doped In2O3 transparent, Appl. Phys. Express 1 (2008) 041501.

[31] T. Koida, H. Fujiwara, M. Kondo, Structural and electrical properties of hydrogen-doped In_2O_3 films fabricated by solid-phase crystallization, J. Non -Cryst. Solids 354 (2008) 2805–2808.

[32] T. Koida, H. Shibata, M. Kondo, K. Tsutsumi, A. Sakaguchi, M. Suzuki, H. Fujiwara, Correlation between oxygen stoichiometry, structure, and opto-electrical properties in amorphous In_2O_3:H films, J. Appl. Phys. 101 (2007) 063705.

[33] J.A. Libera, J.N. Hryn, J.W. Elam, Indium oxide atomic layer deposition facilitated by the synergy between oxygen and water, Chem. Mater. 23 (2011) 2150–2158.

[34] S. Ishibashi, Y. Higuchi, K. Nakamura, Low resistivity indium–tin oxide transparent conductive films. I. Effect of introducing H_2O gas or H_2 gas during direct current magnetron sputtering, J. Vac. Sci. Technol. A 8 (1990) 1399–1402.

[35] P.D.C. King, R.L. Lichti, Y.G. Celebi, J.M. Gil, R.C. Vilão, H.V. Alberto, J. Piroto Duarte, D.J. Payne, R.G. Egdell, I. McKenzie, C.F. McConville, S.F.J. Cox, T.D. Veal, Shallow donor state of hydrogen in In_2O_3 and SnO_2: implications for conductivity in transparent conducting oxides, Phys. Rev. B 80 (2009) 081201R.

[36] S. Limpijumnong, P. Reunchan, A. Janotti, C.G.V. de Walle, Hydrogen doping in indium oxide: an ab initio study, Phys. Rev. B 80 (2009) 193202.

[37] E. Kobayashi, Y. Watabe, T. Yamamoto, High-mobility transparent conductive thin films of cerium-doped hydrogenated indium oxide, Appl. Phys. Express 8 (2015) 015505.

[38] R.D. Shannon, Revised effective ionic radii and systematic studies of interatomic distances in halides and chalcogenides, Acta Cryst. A32 (1976) 751–767.

[39] Y. Shigesato, Y. Hayashi, T. Haranoh, Electrical and structural properties of low resistivity tin-doped indium oxide films, J. Appl. Phys. 71 (1992) 3356–3364.

[40] Y. Shigesato, Y. Hayashi, T. Haranoh, Doping mechanisms of tindoped indium oxide films, Appl. Phys. Lett. 61 (1992) 73–75.

[41] E. Pfender, Electric arcs and arc gas heaters, in: M.N. Hirsh, H.J. Oskam (Eds.), Gaseous Electronics, Vol. 1, Academic, New York, 1978, p. 302.

[42] E. Yanase, I. Watanabe, M. Harada, M. Takahashi, Y. Dake, Y. Hirosima, Probing depth study of conversion electron/He ion yield XAFS spectroscopy on strontium titanate thin films, Anal. Sci. 15 (1999) 255–258.

[43] N. Bassi, C. Clerc, Y. Pelet, J. Hiller, V. Fakhfouri, C. Droz, M. Despeisse, J. Levrat, A. Faes, D. Bätzner, P. Papet, Gridtouch: innovative solution for accurate IV measurement of busbarless cells in production and laboratory environments, in: Proceedings of the 29 the EUPVSEC, Amsterdam, The Netherlands, 2014.

[44] T. Makabe, Z. Petrovic, Plasma, Electronics: Application in Microelectronic Device Fabrication, Taylor & Francis, New York (2006), p. 283.

[45] A. Bianconi, A. Marcelli, H. Dexpert, R. Karnatak, A. Kotani, T. Jo, J. Petiau, Specific intermediate-valence state of insulating 4f compounds detected by L3 x-ray absorption, Phys. Rev. B 35 (1987) 806–811.

[46] K. Oki, Y. Saito, H. Sato, M. Itakura, N. Kuwano, S. Yamashita, T. Yamaguchi, H. Wakita, Intermediate valences of Ce and electrical resistivity changes of Pd-Ce intermetallic compounds, J. Appl. Phys. 69 (1991) 4693–4695.

[47] C.H. Lee, H. Oyanagi, C. Sekine, I. Shirotani, M. Ishii, XANES study of rare-earth valency in LRu_4P_{12} (L=Ce and Pr), Phys. Rev. B 60 (1999) 13253.

[48] G. Niu, M.A. Schubert, F. d'Acapito, M.H. Zoellner, T. Schroeder, F. Boscherini, On the local electronic and atomic structure of $Ce_{1-x}Pr_xO_{2-\delta}$ epitaxial films on Si, J. Appl. Phys. 116 (2014) 123515.